



# Developing a High Ductility Mg Alloy Via Non-basal Slips and Intergranular Coordination Induced by Li and Er Addition

Ruyue Tang<sup>1</sup> · Jing Zhang<sup>1,2</sup> · Bingcheng Li<sup>1</sup> · Quan Dong<sup>1</sup>

Received: 7 October 2023 / Accepted: 27 December 2023 / Published online: 10 February 2024  
© The Author(s) under exclusive licence to The Korean Institute of Metals and Materials 2024

## Abstract

The poor ductility of magnesium (Mg) alloys at room temperature restricts its large-scale usage in industry. In this work, we design low-alloying Mg-3Li- $x$ Er ( $x = 0.2, 0.8$  wt%) alloys with high ductility. Quasi-in-situ electron back-scatter diffraction observation, combined with slip trace analysis and in-grain misorientation axes analysis, was carried out to systematically characterize the microstructural evolution and slip deformation mode during the tensile deformation of the Mg-3Li- $x$ Er alloys. The results showed that the synergy effect of solute Li and Er dramatically reduces the critical resolved shear stress ratios between non-basal and basal slip, thus contributing to the activation of considerable non-basal dislocations. Additionally, Er microalloying increases the frequency of grain boundaries with misorientation angles ( $\theta_s$ ) being in the range of  $75 < \theta_s < 90^\circ$ , enhancing intergranular coordination ability by activating more basal-slip-induced prismatic  $\langle a \rangle$  slips.

**Keywords** Magnesium alloys · Li and Er addition · Ductility · Non-basal slip · Deformation mechanism

## 1 Introduction

Mg alloys have attracted extensive attention in industrial fields for their low density and ease of recycling. However, their low ductility at RT still restricts the scale-up usage of Mg alloys. The hexagonal close-packed (HCP) crystal structure is the essential cause of poor plastic in Mg alloys, which is more likely to activate the basal slip when deformed at RT [1, 2]. Since basal slip only provides a limited slip system and cannot coordinate the strain along the  $c$  direction, increasing the possibility of activating non-basal  $\langle a \rangle$  and  $\langle c + a \rangle$  dislocations, is the critical prerequisite in obtaining desirable plasticity of Mg [3–6]. Furthermore, the ductility of polycrystalline Mg materials depends not only on the activation of slip system, but is also significantly affected by intergranular deformation incompatibility. Therefore, the investigation of slip deformation behavior and intergranular coordination is crucial for developing high ductility Mg alloys.

Numerous theoretical researches indicate that adding proper alloying elements into Mg effectively improves its plastic formability by activating non-basal slip through decreasing the  $c/a$  ratio or stacking fault energy (SFE). For example, Ganeshen et al. [7], showed that adding Al/Ba/Ca/Cu/Li/Y elements decreases the  $c/a$  ratio in different degrees by using first-principles methods. Zhang et al. [8, 9] calculated that all RE elements can reduce  $I_1$  stacking faults, while Li and Zn can ease the  $\{11\text{--}22\}\langle 11\text{--}23 \rangle$  slip system. On the other hand, there are many experimental efforts to illustrate the effect of Li and RE addition on the activation of non-basal slip. Ando et al. [10] and Agnew et al. [11] found many  $\langle a \rangle$  and  $\langle c \rangle$  edge dislocations and high-density  $\langle c + a \rangle$  dislocations distributed in the Mg-Li matrix based on the detailed transmission electron microscope (TEM) analysis. Sandlöbes et al. [12, 13] observed massive pyramidal  $\langle c + a \rangle$  dislocations in solid solution Mg-Y alloys. Further studies have reported that prismatic  $\langle a \rangle$  and pyramidal  $\langle a \rangle$  dislocation slips show more activity in Li/RE-containing alloys compared to pure Mg [14, 15].

As we all know, the slip behavior of dislocations is intensely inhibited by grain boundaries (GBs) and created local stress concentrations detrimental to Mg materials' ductility. Some studies have shown that slip transfer across grain boundaries (i.e., slip-induced slip behavior)

✉ Jing Zhang  
jingzhang@cqu.edu.cn

<sup>1</sup> College of Materials Science and Engineering, Chongqing University, Chongqing 400044, China

<sup>2</sup> National Engineering Research Center for Magnesium Alloy, Chongqing University, Chongqing 400044, China

can effectively release the heterogeneous stress distribution [16–18]. Further studies reported that slip transfer behavior is closely related to the GB disorientation angles ( $\theta_s$ ). For instance, Boehlert et al. [19], reported that most of the slip transfer is more likely to happen at low angle grain boundaries (LAGBs) and GBs with  $\theta_s$  higher than 75 °. Khosravani et al. [20], showed basal-slip-induced extension twinning behavior occurred more easily with  $\theta_s$  of 30 ° ~ 65 °. In addition, Zhao et al. [21] reported that adding dilute Ca and Zn increases the frequency of GBs with  $\theta_s$  lower than 35 °, thus promoting slip transfer across GBs.

Based on the research above, Li and RE elements are the potentially preferred alloying elements to improve the ductility of Mg. Moreover, the solid solubility of Li and RE is much higher than that of most other elements in the Mg matrix [22]. Among rare earth elements, Er elements of high solid solubilities in  $\alpha$ -Mg, with its maximum solid solution being 33.8 wt% [23]. Therefore, ternary Mg-Li-Er is a potential Mg alloy with excellent plasticity. However, the relevant experimental data is rare, and the effect of solutes Li and Er alloying on the activation of non-basal slip and GB disorientation angles deserves further investigation.

In this work, we develop low-alloying Mg-3Li- $x$ Er ( $x=0.2, 0.8$  wt%) ternary alloys with high ductility. Firstly, quasi-in-situ experiments were performed to systematically characterize the microstructural evolution and slip deformation mode during the tensile deformation of the Mg-3Li- $x$ Er alloys. Furthermore, to clarify the mechanism for the high ductility of the Mg-3Li- $x$ Er, the CRSS ratios between non-basal and basal  $\langle a \rangle$  slip ( $\text{CRSS}_{\text{non-basal/basal}}$ ) were estimated by a methodology based on the Schmid factor analysis. In addition, the effect of Er could be explored by comparing the microstructural and activated deformation mode at the same strain of the two different Er-containing alloys with similar grain size and texture type. Hopefully, the work will provide basic data and fundamental knowledge for the design of high-performance Mg alloys, which have crucial scientific research and practical application value.

## 2 Experimental Procedure

### 2.1 Alloy Composition Design and Experimental Materials

According to the purpose of the alloy design in this work, i.e., to reduce the detrimental effect on the ductility brought about by the precipitated particles, the Er concentration was chosen to be at a low level. The Thermo-calc phase diagram calculation software was further used to determine the amount of Er addition. Figure 1 shows the calculated phase fraction diagram of the Mg-3Li- $x$ Er ( $x=0.2, 0.8$  wt%) alloys, respectively. The Mg-3Li-0.2Er alloy is a completely

single-phase  $\alpha$ -Mg, and the Mg-3Li-0.8Er alloy precipitates a small amount of the Mg<sub>24</sub>Er<sub>5</sub> phase, whose mass fraction is 0.6%.

The as-cast Mg-3Li- $x$ Er ( $x=0.2, 0.8$  wt%) alloys were used as raw material, which was synthesized from pure Mg (99.97 wt%), Li (99.90 wt%), and Mg-25 wt% Er master alloys. The actual chemical compositions of the investigated alloys were determined to be Mg-3.01 Li-0.22 Er and Mg-3.02 Li-0.78 Er (wt%) by Inductively Coupled Plasma Optical Emission Spectrometer (ICP). As shown in Fig. 2, the cast ingot has few particles left after homogenizing at 300 °C for 12 h and then water-quenched. Herein, a slightly larger amount of the second phase is distributed in the  $\alpha$ -Mg matrix of the Mg-3Li-0.8Er billets, consistent with the phase diagram calculations.

The two alloys underwent different thermal processing and heat treatment to obtain a similar uniform recrystallized microstructure. For the Mg-3Li-0.2Er alloy, the billet was extruded at 260 °C using an XJ-500 horizontal extruder with an extrusion ratio of 25:1, then annealed at 400 °C for 2 h. The Mg-3Li-0.8Er alloy was extruded at 300 °C and then annealed at 400 °C for 3 h.

### 2.2 The Quasi-in-situ Tensile Tests

The microstructural evolution and slip activities were analyzed by quasi-in situ tensile tests, interrupting the tensile tests and then characterizing the same specimen region under different strains. The tensile test sample was a dog-bone shape plate machined with the length paralleling to the extrusion direction with a gauge of 30.0 mm (L)  $\times$  11.0 mm (W)  $\times$  1.5 mm (T). After grounding and electro-polishing in ethanol – 5% perchloric acid electrolyte for 240 s with direct voltage 20 V and temperature – 30 °C, the initial microstructures of the specimen were characterized by using scanning electron microscopy (SEM, FEI Nova400) equipped with an HKL EBSD system at 20 kV with a step size of 1  $\mu$ m. Then, the specimen was tensile tested to the target strain on a CMT5105 testing machine at RT with a loading velocity of 3 mm min<sup>-1</sup>, and the same region of the deformed specimen was investigated by EBSD and SEM again by appropriate labeling. EBSD data was analyzed by channel 5.0 data acquisition software.

### 2.3 Slip Trace Analysis and IGMA Method

The activated slip deformation mode during tensile plastic deformation was identified by the slip trace analysis and IGMA (in-grain misorientation axes) analysis based on electron backscattered diffraction (EBSD) data. The slip trace analysis enables the determination of the activated slip system by comparing the observed slip lines in grain with all theoretical slip trace directions [24, 25], as shown by the

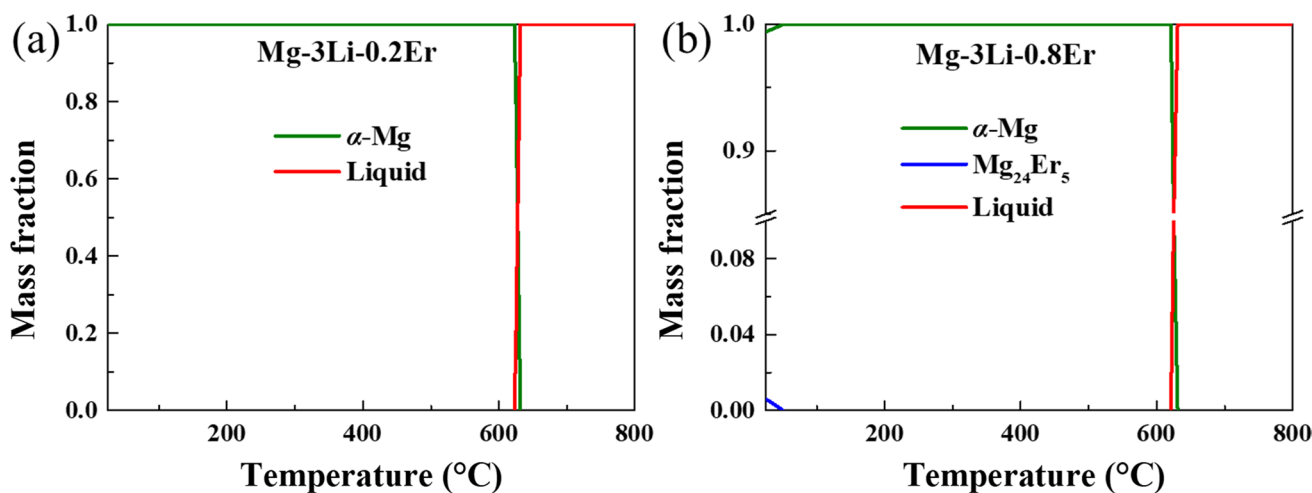


**Fig. 1** Phase fraction diagram of the homogenized alloys: **a** Mg-3Li-0.2Er and **b** Mg-3Li-0.8Er

example in Fig. 3. Figure 3a and b show the SEM image and grain orientation, respectively, of grain (#298) with 3% strain in Mg-3Li-0.2Er alloy. The theoretical slip trace angle was calculated by a self-developed code according to the Euler angle of the target grain, as listed in Fig. 3c. Since the visible slip traces near the grain boundaries are nearly parallel to theoretical slip trace 5, it implies that the  $(01\ 1\ 0) \langle 2\ 110 \rangle$  prismatic  $\langle a \rangle$  slip is activated during deformation. In addition, Fig. 3c displays the Schmid factor corresponding to all 18 theoretical slip systems for grain 298.

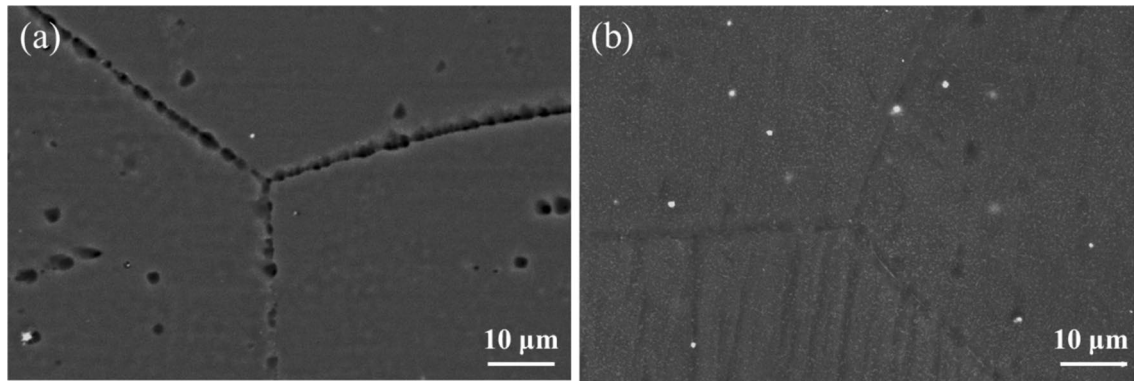
Note that theoretical slip trace direction only provided information about the slip crystal plane. However, some slip systems share the basal or the pyramid I plane  $\{1\ 1\ \bar{0}1\}$ . In this work, if a basal slip line was identified, the basal  $\langle a \rangle$  slip with the largest SF was determined to be activated according to Schmid's law; if a pyramidal I slip line was identified, IGMA analysis was used to identify whether  $\langle a \rangle$  or  $\langle c+a \rangle$  slip system was activated. The IGMA analysis method is based on slip-induced lattice rotation and the determination of its rotation axis (i.e., Taylor axis). According to the Taylor axes corresponding to several typical slip systems of HCP materials [26], the pyramidal I  $\langle a \rangle$  slip and pyramidal I  $\langle c+a \rangle$  slip would trigger rotation about  $\langle 0\ 1\ 12 \rangle$  axis and  $\langle 13\ 85\ 3 \rangle$  axis, respectively. The activated dislocation type can therefore be determined by the distribution of polar density in grains with apparent pyramid I slip trace. In this work, the misorientation axes of material-point pairs with misorientation between  $0.5^\circ$  and  $2^\circ$  are plotted, and the pole density is calculated.

### 3 Results

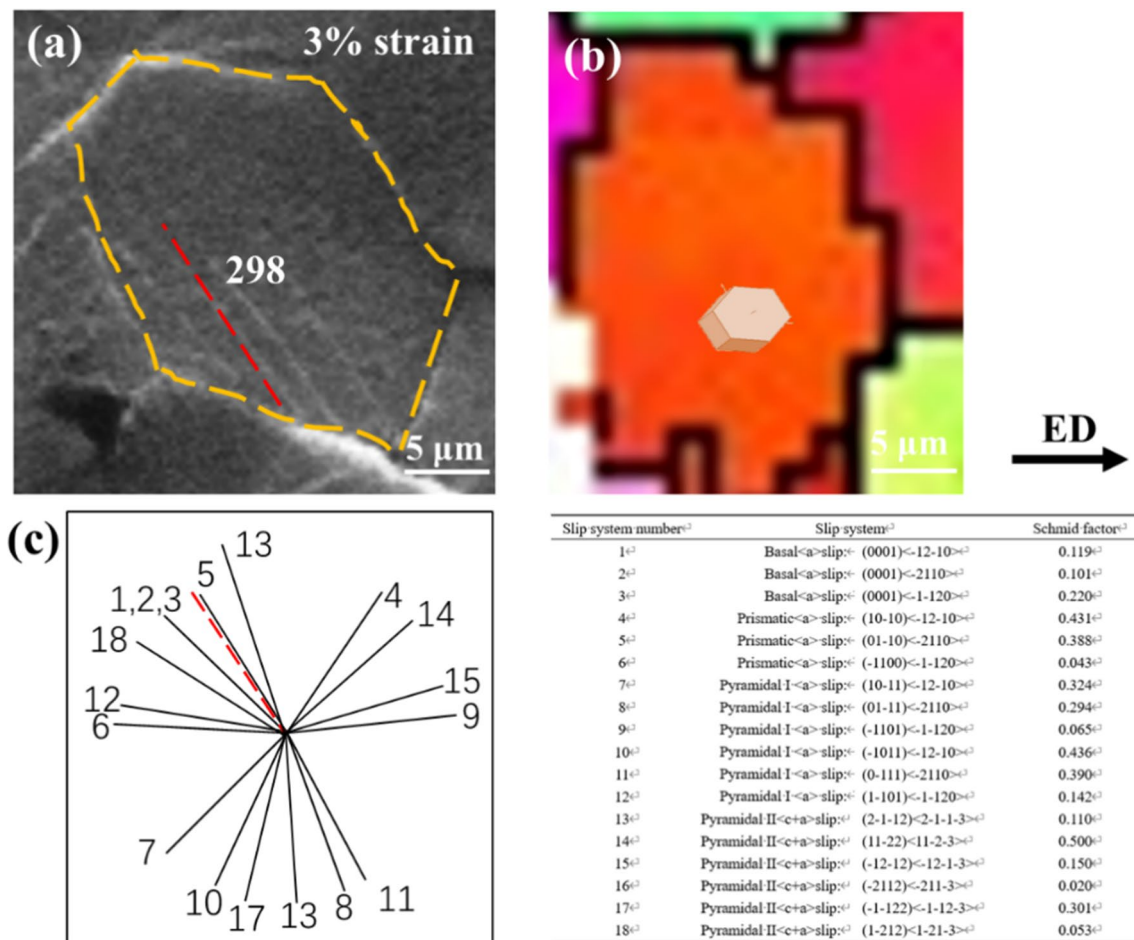
#### 3.1 Microstructures and Mechanical Properties of Mg-3Li-xEr Alloys

Figure 4a and b display the inverse pole figures (IPF) and grain size distribution maps of the as-annealed Mg-3Li-xEr ( $x=0.2, 0.8$  wt%) alloys. As shown in Fig. 4a and b, the as-annealed grains are approximately equiaxed and no twin structure is observed. The grain size distribution maps show that the as-annealed Mg-3Li-0.2Er and Mg-3Li-0.8Er alloys have a uniform size distribution, and the average grain size of both alloys are about  $19\ \mu\text{m}$ . After sorting and labeling, it was determined that the selected areas containing 633 and 625 complete grains for the Mg-3Li-0.2Er and Mg-3Li-0.8Er alloys, respectively. Figure 4c and d show the  $\{0001\}$ ,  $\{11\ \bar{2}\ 0\}$  and  $\{10\ \bar{1}\ 0\}$  pole figures of the as-annealed Mg-3Li-xEr ( $x=0.2, 0.8$  wt%) alloys. The annealed Mg-3Li-0.2Er alloy exhibits a texture having a splitting of basal poles along the TD, which is apparently a typical fiber texture type, and is in agreement with other Mg-Li/Mg-RE results that have been reported [27, 28]. With the increase of Er content, the polar density of the (0001) polar axis in the TD direction is weakened, in place of which there is a clear inclination in the ED direction, and the maximum texture intensity decreases from 5.71 (mrd) to 4.31 (mrd), which implies that the minor addition of Er weakens the texture intensity of the alloys.

Figure 5a and b show the tensile engineering stress–strain curves and the corresponding tensile properties of the as-annealed Mg-3Li-xEr ( $x=0.2, 0.8$  wt%) alloys. The ultimate tensile strength and elongation of the Mg-3Li-0.2Er alloy are 141 MPa and 17.0%, respectively. The strength of the Mg-3Li-0.8Er alloy is the same as that of the Mg-3Li-0.2Er



**Fig. 2** SEM images of the homogenized alloys: **a** Mg-3Li-0.2Er and **b** Mg-3Li-0.8Er



**Fig. 3** Example illustrating the slip trace analysis method: **a** SEM image of grain 298 after 3% strain in Mg-3Li-0.2Er alloy (the red dash line represents the real observed slip traces) and **b** the IPF map

at the same region; **c** all 18 theoretical slip trace directions and the corresponding SFs for grain 298

alloy, but the higher Er-containing alloy has a higher elongation (24.1%), with a significant increase of about 40%. The above results suggest that Er solute greatly enhances the ductility of the alloys, noting that the secondary phases

are minimal and the microstructures (grain size and texture) are very similar for both as-annealed alloys. Based on the stress–strain curves, quasi-in-situ tensile tests were carried out at selected strains of 3%, 8%, and 16%, as labeled in

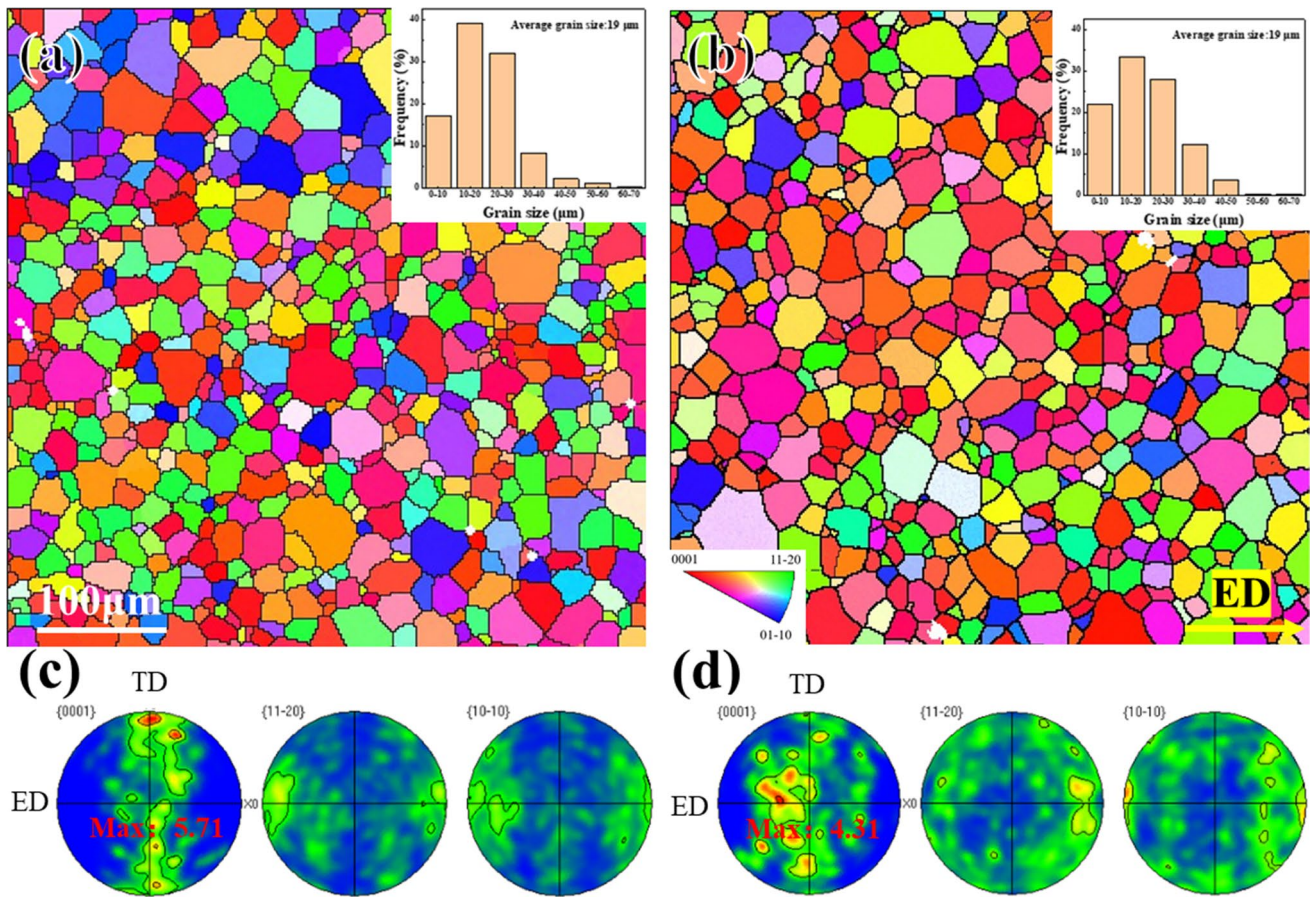


Fig. 4 IPF maps, grain size distribution maps and pole figures of the as-annealed alloys: **a, c** Mg-3Li-0.2Er and **b, d** Mg-3Li-0.8Er

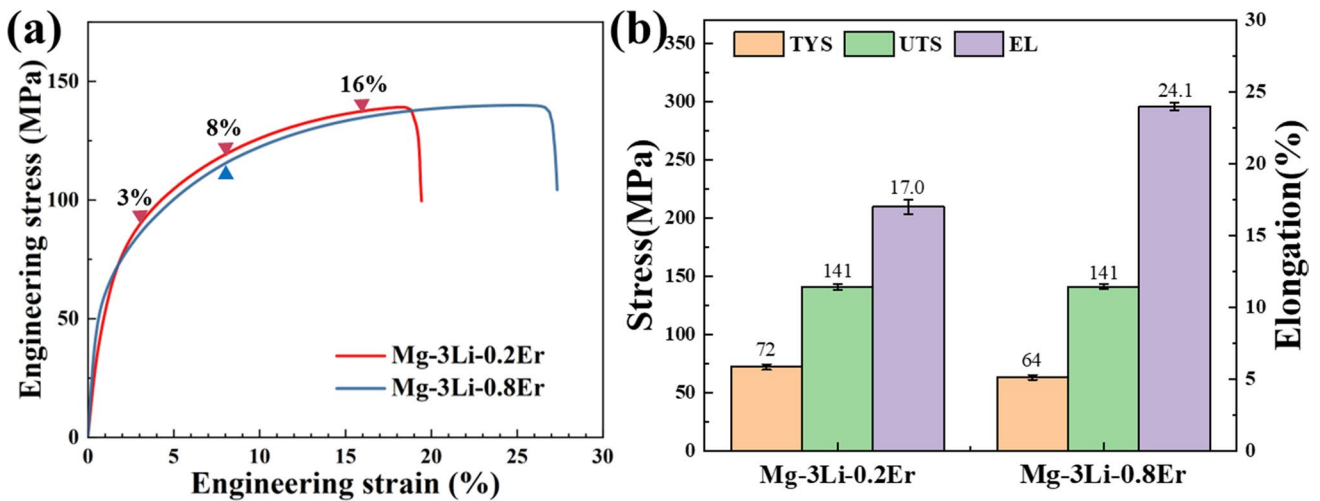
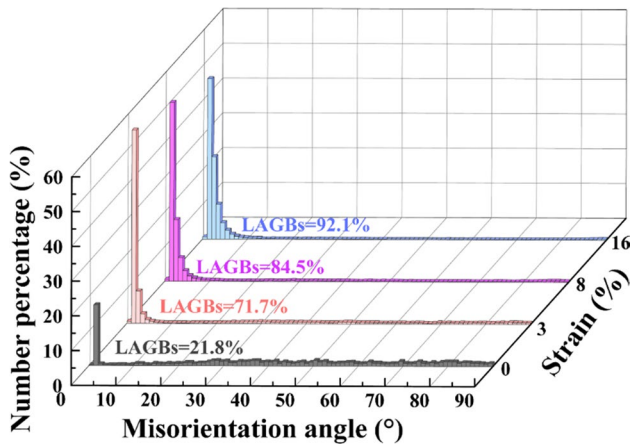


Fig. 5 **a** Tensile engineering stress–strain curves and **b** mechanical properties of the as-annealed alloys

Fig. 5a, which represents three typical deformation stages of near yielding, uniform plastic deformation, and approaching fracture, respectively.

### 3.2 Quasi-in-situ Tensile test of Mg-3Li-0.2Er Alloy

#### 3.2.1 Evolution of Misorientation Angle Distribution



**Fig. 6** Misorientation angle distributions of the Mg-3Li-0.2Er alloy at different tensile strains

boundary ( $<15^\circ$ ) increases dramatically, resulting in a high number percentage of LAGBs (71.7%). In the meantime, it is noted that there are no peaks around  $86^\circ$  and  $56^\circ$ , indicating that very little twinning occurs during the tensile deformation. The number percentage of LAGBs increases gradually with increasing strains, around 92.1% at 16% strain. The increase in LAGBs is contributed to the more dislocations slip, which means slip behavior is the predominant deformation mode during the tensile plastic deformation of the Mg-3Li-0.2Er alloy.

Figure 7 shows the  $\{0001\}$  and  $\{10\bar{1}0\}$  pole figures of the Mg-3Li-0.2Er alloy at different tensile strains. The TD-texture component changes during tension in the  $\{0001\}$  pole figures. Upon increasing strains, the maximum intensities of the TD-texture component increase from 5.68 (mrd) to 7.03 (mrd). Meanwhile, another texture component near this texture deflects to TD, where the maximum intensities

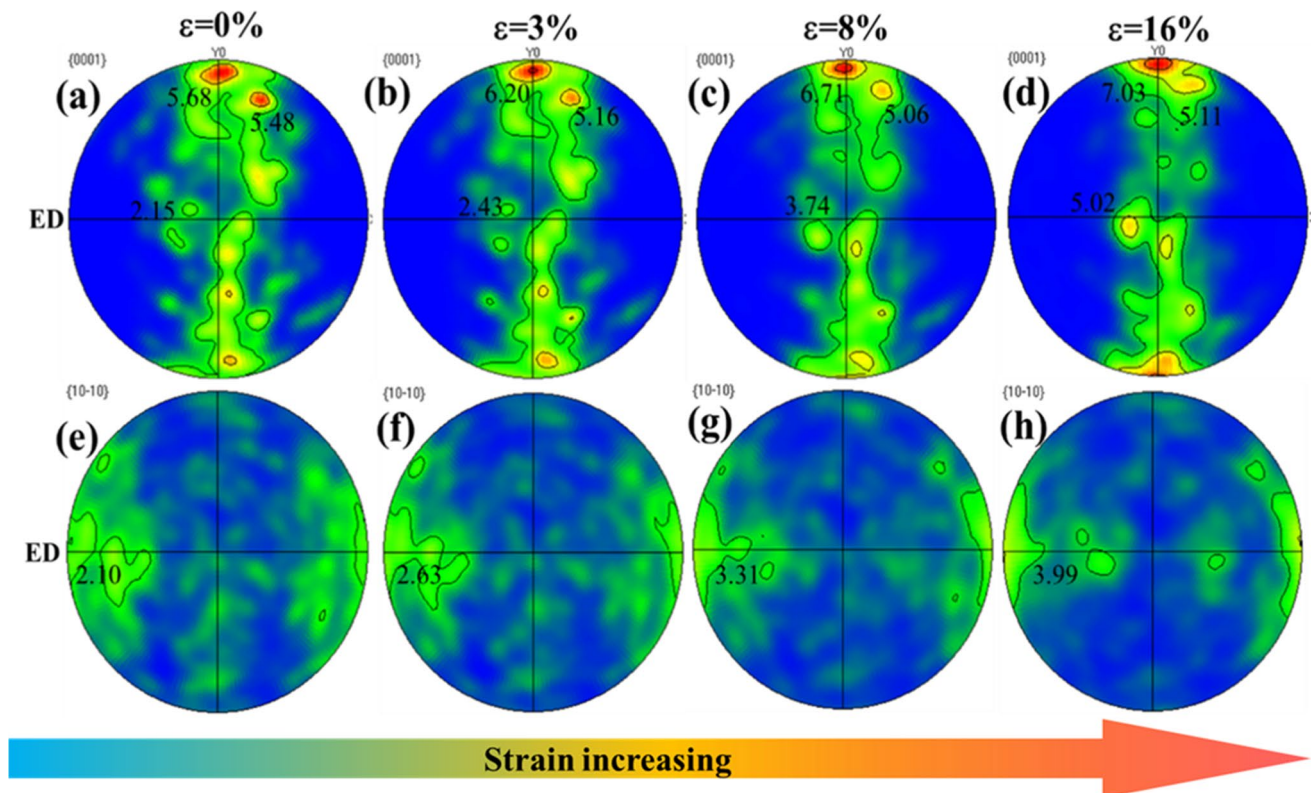


**Fig. 7**  $\{0001\}$  and  $\{10\bar{1}0\}$  pole figures of the Mg-3Li-0.2Er alloy at different tensile strains

### and Texture

Figure 6 shows the misorientation angle distribution of the as-deformed Mg-3Li-0.2Er alloy at different interrupting tensile strains. Before tensile deformation, the misorientation angle is evenly distributed, and most grains are HAGBs ( $>15^\circ$ ). At the strain of 3%, the number of low angles grain

gradually weakened from 5.48 (mrd) to 5.11 (mrd). Furthermore, the  $<10-10>$  // ED orientation texture intensities increase monotonously with increasing strains (Fig. 7e–h). The above texture evolution indicates that the prismatic  $<a>$  slip is continuously initiated during tensile deformation [29]. Besides, a weak-texture component with basal

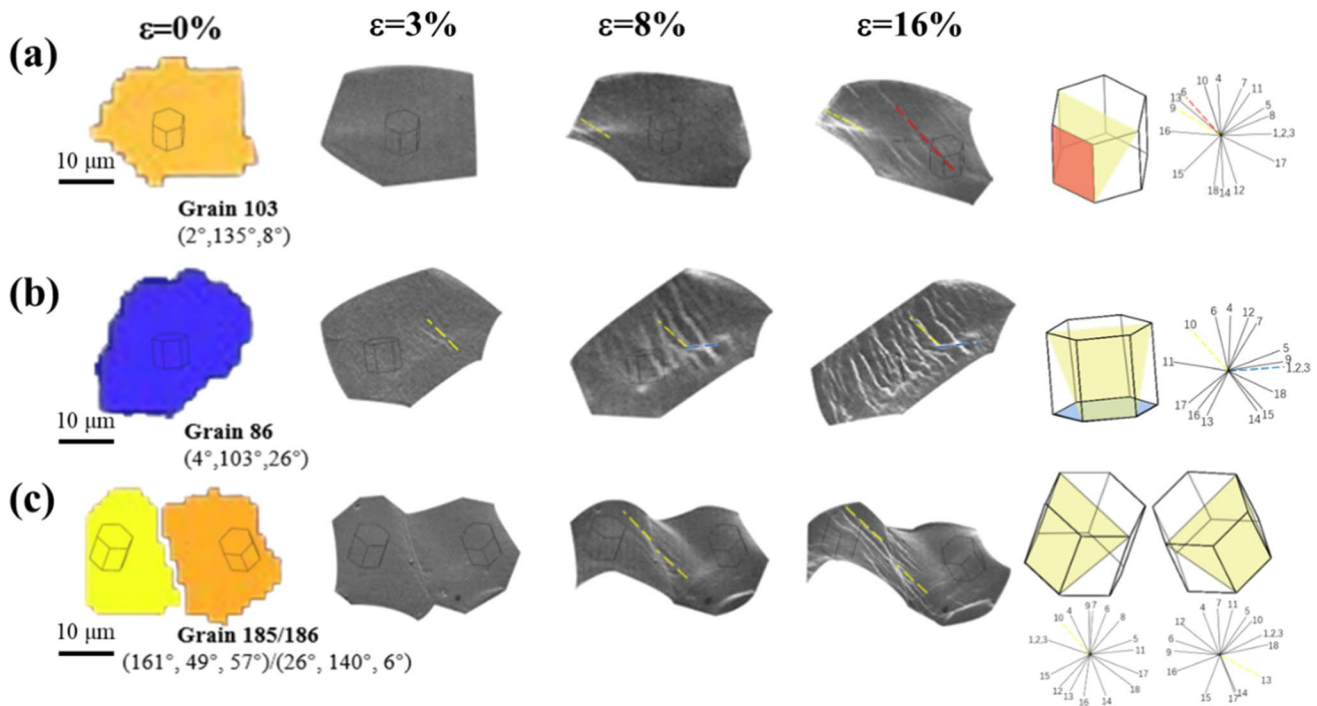


**Fig. 8** Grain orientations of three groups of grains (103, 86, 185/186) and the actual observed slip traces at different tensile strains. The slip planes of identified slip systems labelled with different color and theoretically calculated slip directions are shown on the right

plane parallel to the ED is formed, and its maximum strength increases from 2.15 (mrd) to 5.02 (mrd) (Fig. 7a–d). Additional deformation mechanisms that can contribute to the ED-texture component are the increase of pyramid  $\langle c+a \rangle$  slip [30] or  $\{10\bar{1}1\}\{10\bar{1}2\}$  double twinning [31]. Given that there is a low percentage of twinning activation, it can be deduced that the pyramid  $\langle c+a \rangle$  slip is attributed to the formation of the ED-texture component. In other words, this result reveals that pyramid  $\langle c+a \rangle$  slip can be gradually activated during the tensile deformation of the Mg-3Li-0.2Er alloy. The misorientation angle distribution and texture evolution illustrate that more slips/non-basal slips are initiated during the tensile deformation with larger strain.

### 3.2.2 Evolution of the Actual slip Trace

Figure 8 shows three examples of the evolution of the actual non-basal/basal slip lines within the grains (103, 86, 185/186) of the Mg-3Li-0.2Er alloy, including multiple-slip, cross-slip, and intergranular coordination.

Grain 103 displays the development of the multiple-slip system with increasing strains. The slip lines (marked by a yellow dashed line) are the theoretical pyramidal I  $\langle a \rangle$  slip traces that form near the grain boundary and become denser with tensile strain increasing. Subsequently, another slip line

in the middle of the grain (marked by a red dashed line) corresponding to activating the prismatic  $\langle a \rangle$  slip system becomes visible when the strain reaches 16%.

Grain 86 demonstrates the cross-slip process of  $\langle a \rangle$  dislocations. Firstly, the sets of slip lines that belong to the pyramidal I  $\langle a \rangle$  slip system were observed after 3% strain, and the slip lines (marked by a white dashed line) determined as basal  $\langle a \rangle$  slip system appears at the intersection of pyramidal I  $\langle a \rangle$  slip trace when the deformation further increasing. The screw  $\langle a \rangle$  dislocations slip between the basal plane and pyramidal I plane without changing the slip direction, which allows for greater flexibility in dislocation movement and facilitates plastic deformation of the alloy.

Grains 185 and 186 show the intergranular coordination processes during the tensile deformation. When the strain is 8%, a small amount of slip lines are observed at the grain boundaries between grain 185 and grain 186, and both sets of slip lines are identified as the pyramidal I  $\langle a \rangle$  slip system. The slip traces penetrate grain 185 after 16% strain, while the slip lines within grain 186 only appear near the grain boundary, implying more significant deformation within grain 185. Therefore, it can be speculated that the activation order of the slip mode of the two grains (185/186) is as follows: Firstly, the pyramidal I  $\langle a \rangle$  slip system is activated in grain 185, and then stress concentration is caused at the grain boundary, followed by the activation of the

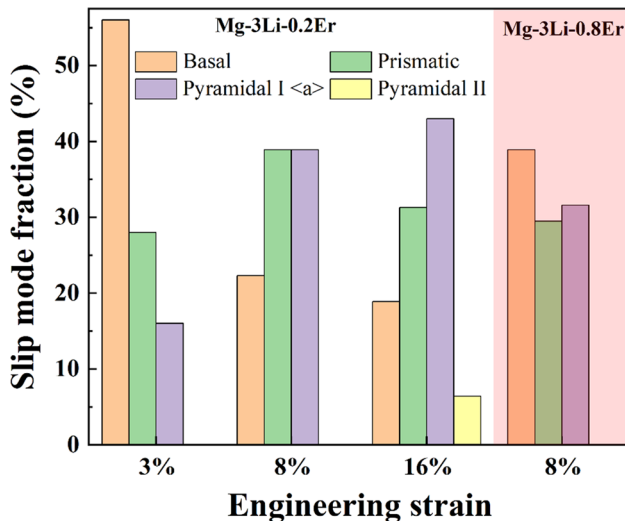


**Fig. 9** Statistics on the activation of different slip modes in Mg-3Li- $x$ Er ( $x=0.2, 0.8$  wt%) alloys at various tensile strains

pyramidal I  $\langle a \rangle$  slip system within grain 186 because of the slight orientation difference between grain 185 and grain 186.

### 3.3 Statistical Analysis of Slip Activity of Mg-3Li- $x$ Er Alloys

According to the aforementioned qualitative analysis, more slips/non-basal slips are initiated with increasing strain. The evolution of the slip trace during the quasi-in-situ tensile test is further discussed quantitatively by slip trace analysis. Figure 9 shows the activated fraction of different slip systems of the Mg-3Li- $x$ Er alloys at various tensile strains. More specific parameters are shown in Table 1. The fraction is the line number of individual identified slip systems divided by the number of observed total slip lines. As shown in Table 1, slip lines are visible in 25, 121, and 265 grains after 3%, 8%, and 16% strains, respectively, in the Mg-3Li-0.2Er specimen. Since some grains develop more than one type of slip line due to multiple-slip and cross-slip, the identified slip number is higher than the grain number. At the strain of 3%, the fraction of basal  $\langle a \rangle$  slip accounts for 56% of all visible slip traces, indicating that it's the predominated deformation mode in the early stages of deformation. As the strain increases to 8%, sizable non-basal slip traces are identified, and the fractions of prismatic  $\langle a \rangle$  slip and pyramid I  $\langle a \rangle$  slip are both 38.9%. The fraction of slip lines at 16% strain is similar to that at 8% strain, with a slightly higher fraction of non-basal slip lines. Compared with Mg-3Li-0.2Er alloy, Mg-3Li-0.8Er alloy shows a somewhat lower ratio of non-basal slip traces at 8% strain, with the fraction of prismatic  $\langle a \rangle$  slip and pyramid I  $\langle a \rangle$  slip lines being 29.5% and 31.6%, respectively.

Since the slip traces which are identified as the pyramidal I slip used by slip trace analysis may be caused by either  $\langle a \rangle$  or  $\langle c+a \rangle$  dislocations slip, IGMA analysis is used to determine the specific slip system in the pyramid I plane ( $\{1\bar{1}01\}$ ). The grains with apparent pyramid slip lines of Mg-3Li-0.2Er alloy are selected for IGMA analysis to determine the pyramid I slip system as an example. Since possible errors exist, the analysis results of the activated slip mode identified by the slip trace analysis and IGMA methods may sometimes differ. The IGMA distribution of the grains in which consistent results are determined is divided into two types: one type of grains tends to develop  $\langle 0\bar{1}12 \rangle$  axis distribution, in which the dominant plastic deformation mode is pyramidal I  $\langle a \rangle$  slip, as shown in Fig. 10a. The other grains with IGMA concentrated near the  $\langle 0\bar{1}12 \rangle$  axis and  $\langle 13853 \rangle$  axis are predominated by pyramidal I  $\langle a \rangle$  slip and pyramidal I  $\langle c+a \rangle$  slip, as shown in Fig. 10b. However, no grains develop their IGMA only concentrated near the  $\langle 13853 \rangle$  axis.

The results of IGMA shown in Fig. 10 illustrate that the dominant slip mode is pyramidal I  $\langle a \rangle$  slip, further verified by Schmid's law. Figure 11 displays the highest SFs for pyramidal I  $\langle a \rangle$  slip and pyramidal I  $\langle c+a \rangle$  slip of above grains, and the results show that SFs for pyramidal I  $\langle a \rangle$  slip are larger than those for  $\langle c+a \rangle$  slip system in most of the grains (76%). In addition, there are a few grains with similar SFs for pyramidal I  $\langle a \rangle$  slip as those of the  $\langle c+a \rangle$  slip, and yet only one grain with larger SFs for pyramidal I  $\langle c+a \rangle$  slip. Combined with IGMA analysis results, we consider the identified pyramidal I slip trace to be pyramidal I  $\langle a \rangle$  slip.

## 4 Discussion

In this work, the as-annealed Mg-3Li- $x$ Er ( $x=0.2, 0.8$  wt%) alloys exhibit high plasticity at room temperature. The slip trace analysis confirmed that substantial non-basal slips can be activated in the middle and late stages of the tensile deformation. Besides, compared to the Mg-3Li-0.2Er alloy, the Mg-3Li-0.8Er alloy with similar microstructure shows a higher elongation and a significant increase in EL by about 40%. The mechanism underlying the high flexibility of the Mg-3Li- $x$ Er ( $x=0.2, 0.8$  wt%) alloys and considerable enhancement of flexibility by Er microalloying needs further discussion and analysis.

### 4.1 Ductility and Non-basal of Mg-3Li- $x$ Er Alloys

As for Mg alloys, the CRSS ratio between non-basal and basal ( $CRSS_{non-basal}/CRSS_{basal}$ ) is an influential parameter affecting their ductility. In general, the materials with lower



**Table 1** Specific statistics on the activation of different slip modes in Mg-3Li-0.2Er alloy at various tensile strains

Strain (%)	Grain (number/fraction)	Total slip traces			Slip traces (number/fraction)		
		Basal (%)	Prismatic (%)	Pyramidal I (%)	Basal (%)	Prismatic (%)	Pyramidal II (%)
3	25/3.9	14/56.0	7/28.0	4/16.0	0/0	0/0	0/0
8	100/15.8	27/22.3	47/38.9	47/38.9	0/0	0/0	0/0
16	190/30.0	50/18.9	83/31.3	114/43.0	17/6.4	17/6.4	17/6.4

CRSS ratios exhibit better plastic deformation ability. It has been reported that the ratios of  $CRSS_{non-basal}/CRSS_{basal}$  in pure Mg are up to 40–160, which is the fundamental reason for its poor ductility [32]. Based on the experimental phenomena, i.e., the high ductility and considerable non-basal slip traces in Mg-3Li-0.2Er and Mg-3Li-0.8Er alloys, it is necessary to calculate the CRSS ratios of these alloys.

H. Li et al. proposed a methodology to estimate the CRSS ratios, which are introduced as follows [33]. Using the Mg-3Li-0.2Er specimen as an example, 100 grains with slip traces at the strains of 8% are analyzed. Figure 12a shows the identified 121 deformation slip systems and Schmid factor distribution in all 100 grains, which were categorized by 0.05 Schmid factor increments. 12 possible slip systems are taken into consideration, including 3 basal  $\langle a \rangle$  slip systems, 3 prismatic  $\langle a \rangle$  slip systems, and 6 pyramidal I  $\langle a \rangle$  slip systems. This defines a matrix where the value for each pair (i, j) is denoted as  $N_{ij}$  (i = 1, ..., 10, j = 1, 2, 3). And 1200 potential deformation systems to be analyzed in the same manner as described for Fig. 12a can be denoted  $D_{ij}$ , as shown in Fig. 12c. Since the activation of slip system in one grain mainly depends on the SF and the CRSS of each slip system, firstly, assuming the same CRSS for all deformation systems, a cubic weighting function (Eq. (1)) is applied to reduce the influence of the SF on the slips activity, resulting in the matrix  $W_{ij}$ ; Then the assumed CRSS values and least-square minimization are adopted to optimize the CRSS ratios. During the optimization, the squared difference  $d(\tau_1, \tau_2, \tau_3; c)$  can be calculated by Eq. (2), and the “optimal” values for the CRSS values are calculated by solving the first-order derivative conditions for  $d(\tau_1, \tau_2, \tau_3; c)$  as shown in Eq. (3). The  $P_{ij}^0$  represents the expected number of observations of deformation type j and Schmid factor bin i and  $P_{ij}$  is a matrix based on the  $P_{ij}^0$  results which takes into account the true CRSS of deformation system.

$$W_{ij} = D_{ij}((i - 1)/9)^3 \tag{1}$$

$$d(\tau_1, \tau_2, \tau_3; c) = \sqrt{\sum_{i,j=1}^{10,3} (P_{ij} - N_{ij})^2} = \sqrt{\sum_{i,j=1}^{10,3} \left(\frac{c}{j} P_{ij}^0 - N_{ij}\right)^2} \tag{2}$$

$$\frac{cd}{c_j} = 0 \rightarrow j = c \frac{\sum_1^m (p_{ij}^0)^2}{\sum_{i=1}^m N_{ij} P_{ij}^0} \tag{3}$$

Where  $\tau_1, \tau_2,$  and  $\tau_3$  are the “optimal” CRSS values for basal  $\langle a \rangle,$  prismatic  $\langle a \rangle,$  and pyramidal I  $\langle a \rangle$  slip system, respectively, and c is an unknown parameter, which does not affect the CRSS ratio calculation.

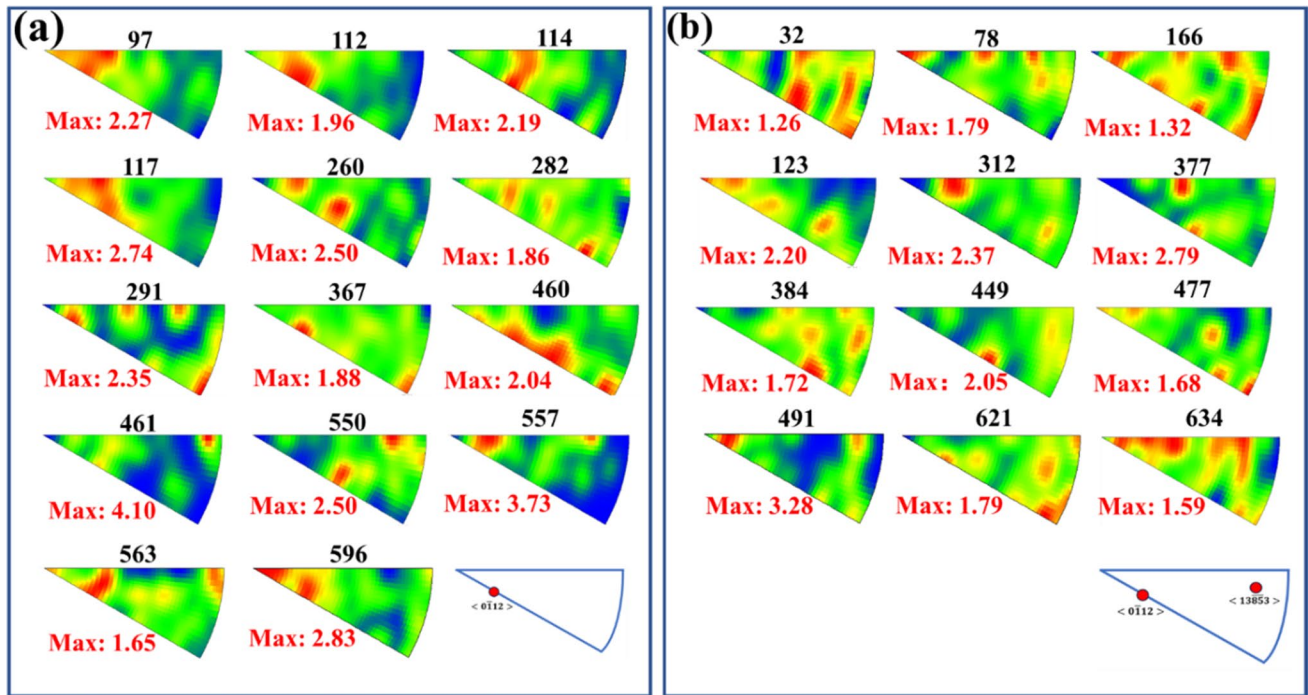


**Fig. 10** **a** Grain with IGMA only concentrated on the  $\langle 0 \bar{1} 12 \rangle$  axis and **b** grain with IGMA concentrated on the  $\langle 0 \bar{1} 12 \rangle$  and  $\langle 1 \bar{3} \bar{8} 5 \bar{3} \rangle$  axis

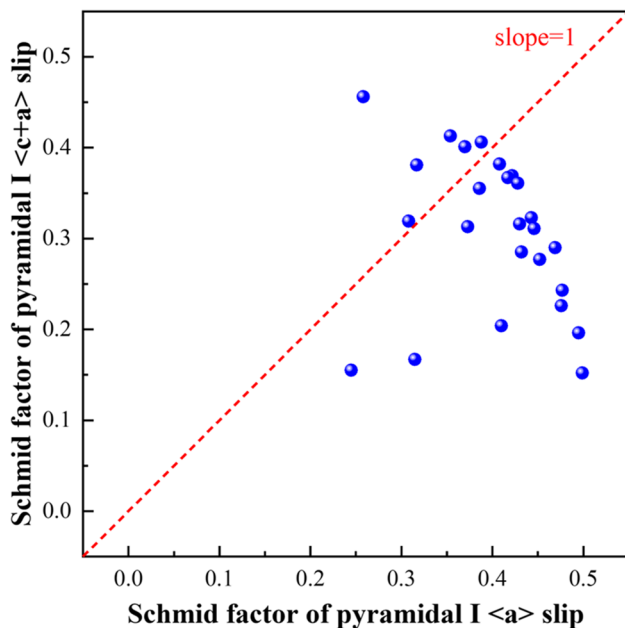


**Fig. 11** Schmid factors for pyramidal I  $\langle a \rangle$  slip and pyramidal I  $\langle c+a \rangle$  slip for grains with pyramidal I slip lines

According to the method above, the optimal theoretical Schmid factors distribution is shown in Fig. 12e, which almost follows the experimental Schmid factors distribution (shown in Fig. 12a). Accordingly, optimal parameters,  $\tau_1$ ,  $\tau_2$ ,

and  $\tau_3$ , can be obtained as 0.61c, 0.78c, and 1.38c, respectively. Therefore, the  $\text{CRSS}_{\text{prism}}/\text{CRSS}_{\text{basal}}$  and  $\text{CRSS}_{\text{py I } \langle a \rangle}/\text{CRSS}_{\text{basal}}$ , i.e.,  $\tau_2/\tau_1$  and  $\tau_3/\tau_1$ , are calculated to be 1.29 and 2.27, respectively.

For the Mg-3Li-0.8Er alloy, using the same method as the Mg-3Li-0.2Er alloy, the calculated  $\tau_1$ ,  $\tau_2$ , and  $\tau_3$  are 0.46c, 0.98c, and 1.66c, respectively. Thus, the  $\text{CRSS}_{\text{prism}}/\text{CRSS}_{\text{basal}}$  and  $\text{CRSS}_{\text{py I } \langle a \rangle}/\text{CRSS}_{\text{basal}}$  can be obtained as 2.13 and 3.59, respectively. Figure 12b, d, and f show the experimentally observed, potential, and predicted activated deformation system–Schmid factor distribution of the Mg-3Li-0.8Er alloy, respectively. Based on the above calculation results, it can be seen that the  $\text{CRSS}_{\text{non-basal}}/\text{CRSS}_{\text{basal}}$  of Mg-3Li- $x$ Er ( $x=0.2, 0.8$  wt%) alloys are much lower than that of pure Mg and other commercial Mg alloys [24, 34, 35], implying that the addition of Li and Er elements can dramatically reduce the CRSS of non-basal slips.

#### 4.2 Mechanisms of Er Microalloying on the Ductility

According to the slip trace analysis, compared with Mg-3Li-0.2Er alloy, Mg-3Li-0.8Er alloy shows a lower fraction of non-basal slip lines at the 8% strain. It is noted that the counts of Schmid factors higher than 0.25 in the two alloys after a plastic strain of 8% is 60 and 80, respectively, and the Mg-3Li-0.8Er alloy has a larger proportion of high Schmid

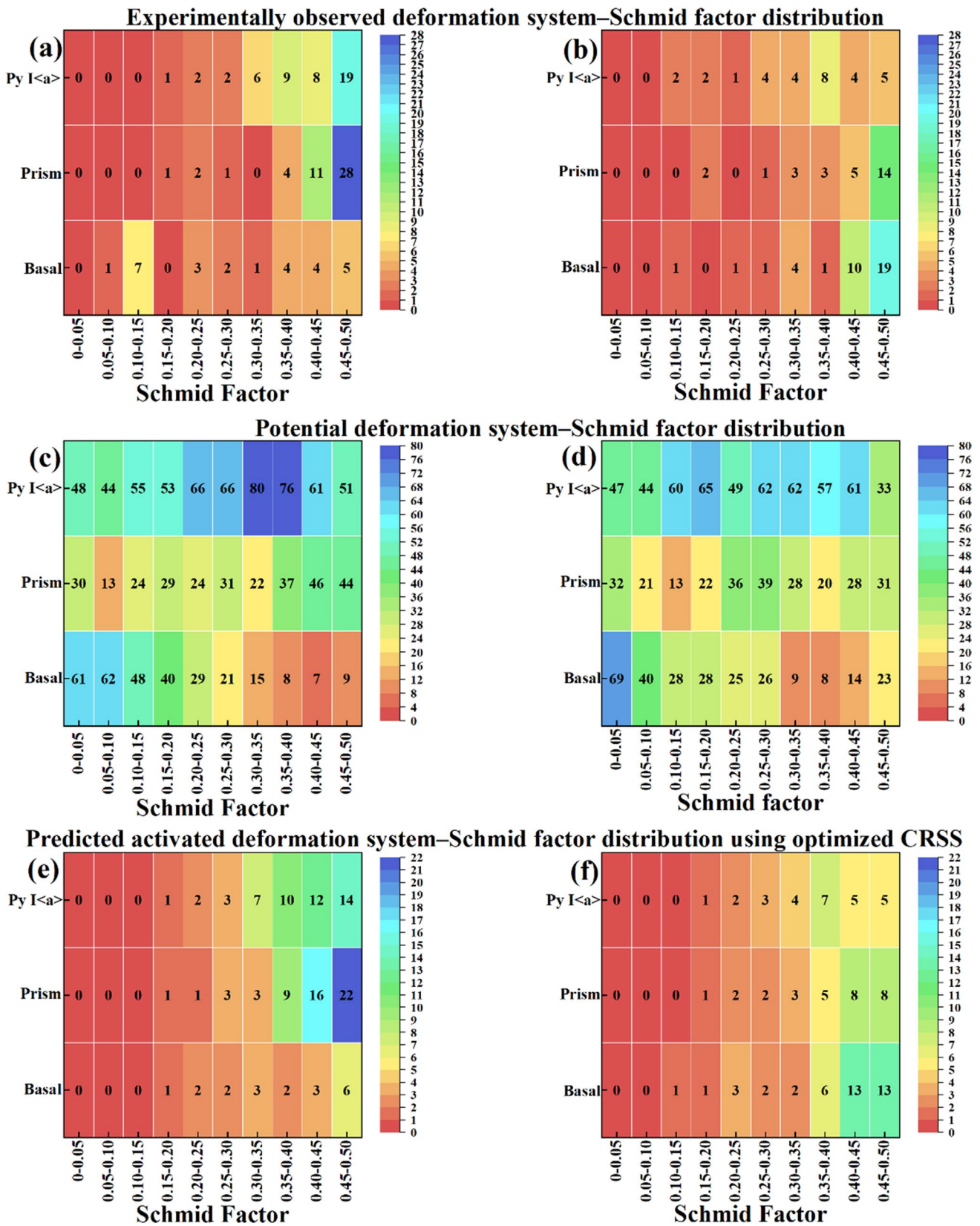


**Fig. 12** Experimentally observed deformation system–Schmid factor distribution, potential deformation system–Schmid factor distribution, and predicted activated deformation system–Schmid factor dis-

tribution using optimized CRSS ratios of Mg-3Li-0.2Er **a, c, e** and Mg-3Li-0.8Er **b, d, f** alloys, respectively

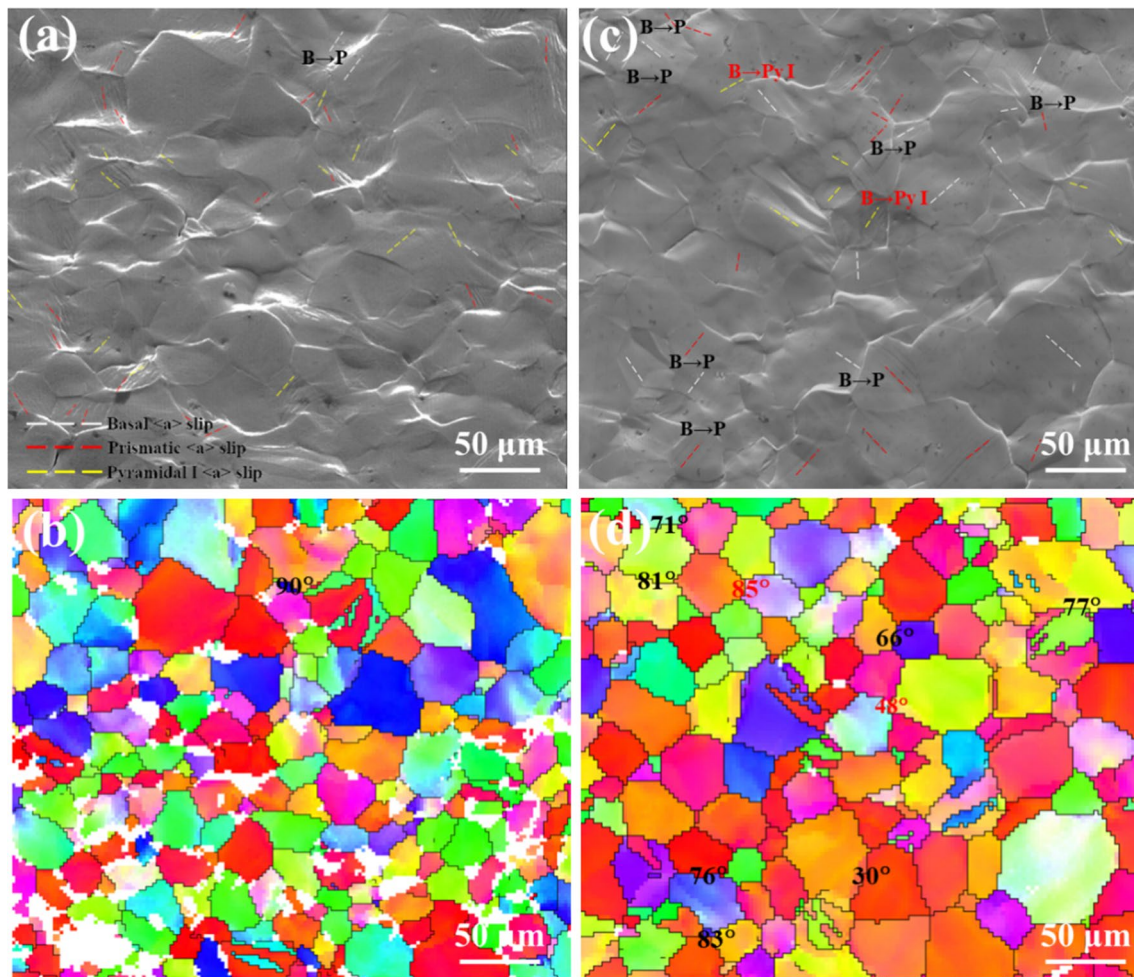


**Fig. 13** SEM images of visible slip traces and corresponding IPF in the **a, b** Mg-3Li-0.2Er and **c, d** Mg-3Li-0.8Er alloys at 8% tensile strain. Basal-slip-induced non-basal slip events are labeled in SEM images, where the black B→P markers represent the basal-

slip-induced prismatic  $\langle a \rangle$  slip events and the red B→Py I markers represent basal-slip-induced pyramidal I  $\langle a \rangle$  slip events; The corresponding  $\theta_s$  of the basal-slip-induced non-basal  $\langle a \rangle$  slips are shown in IPF map with different color, respectively

factor for basal slip ( $m_{\text{basal}}$ ) (Fig. 12c and d), which indicates more diffuse texture grains with high  $m_{\text{basal}}$  can be obtained with Er microalloying. Bearing in mind that the CRSS of the basal slip system is the lowest and always the easiest to be activated, the increased elongation of the Mg-3Li-0.8Er alloy is therefore deemed to be partly influenced by the easier initiation of basal slip, especially in the initial deformation stage, where the basal slip can accommodate more plastic deformation at lower stress.

Additionally, intergranular coordination plays a crucial role in the plastic deformation stage of polycrystals [36, 37]. The slip transferring behaviors across GBs, i.e., slip-induced slip behavior, can improve flexibility by effectively alleviating local stress concentrations near GBs [38]. It is generally believed that intergranular coordination is caused by basal  $\langle a \rangle$  slip because of its minimal CRSS. Figure 13a and c display the visible slip traces of the

Mg-3Li- $x$ Er ( $x=0.2, 0.8$  wt%) alloys after 8% strain, with the dashed lines of different colors representing the other slip systems activated. As shown in Fig. 13a and b, in the Mg-3Li-0.2Er alloy, only one possible basal-slip-induced non-basal slip event is observed. However, more basal-slip-induced non-basal slip events can be visible in the Mg-3Li-0.8Er alloy, most of which belong to basal-slip-induced prismatic  $\langle a \rangle$  slip events. It has been reported [19] that slip transfer behavior was associated with GB misorientation angles ( $\theta_s$ ), and the  $\theta_s$  of the basal-slip-induced prismatic  $\langle a \rangle$  slip was reported recently to be 75–90° in the Mg–Y alloy by Zhou et al. [17]. In our case, as shown in the IPF maps (Fig. 13c and d), a large number of the basal-slip-induced prismatic  $\langle a \rangle$  slip events appear with  $\theta_s$  of 66–90°, and only one event happens at GB with lower  $\theta_s$  (30°). Figure 14 shows the histograms of misorientation distribution in the Mg-3Li- $x$ Er ( $x=0.2,$

0.8 wt%) alloys. The frequency of GBs with  $75^\circ < \theta_s < 90^\circ$  of the two alloys are 15.7% and 18.6%, respectively. The larger frequency of GBs with  $75^\circ < \theta_s < 90^\circ$  in the Mg-3Li-0.8Er alloy suggests that the basal-slip-induced prismatic  $\langle a \rangle$  slip behavior is more favorable, and therefore, the possibility of activating more potential slip systems is greater in the Mg-3Li-0.8Er alloy. (Fig. 14)

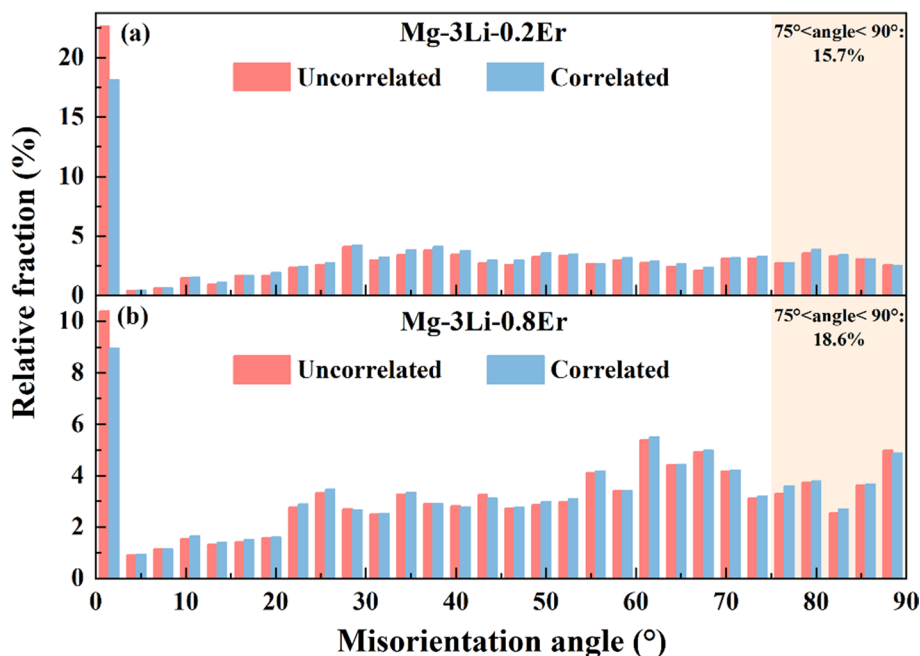
Combined with the results of a higher fraction of basal slip lines in the higher Er-containing alloy, it can be concluded that the Mg-3Li-0.8Er alloy exhibits better intergranular coordination ability than the Mg-3Li-0.2Er alloy. The Kernel Average Misorientation (KAM) maps of Mg-3Li- $x$ Er ( $x = 0.2, 0.8$  wt%) alloys (Fig. 15) further validated that the strain distribution in the Mg-3Li-0.8Er alloy is more uniform compared with that in the Mg-3Li-0.2Er alloy. As a result, Er microalloying enhances alloy ductility due to easier basal  $\langle a \rangle$  slip as well as more active basal-induced prismatic  $\langle a \rangle$  slip behavior.

## 5 Conclusion

In this work, the deformation mechanisms of the Mg-3Li- $x$ Er ( $x = 0.2, 0.8$  wt%) alloys under tension at RT were studied by quasi-in situ EBSD tests combined with slip trace analysis and IGMA analysis. The main conclusions are as follows:

- (1) Basal slip is the predominant deformation mode in the initial deformation stage, and considerable non-basal slips are activated in the middle and late stages of tensile deformation. When the strain reaches 16%, the fractions of basal  $\langle a \rangle$ , prismatic  $\langle a \rangle$ , pyramidal I  $\langle c \rangle$ , and pyramidal II  $\langle c + a \rangle$  slip in the Mg-3Li-0.2Er alloy are 18.9%, 31.3%, 43.0%, and 6.4%, respectively.
- (2) As-annealed Mg-3Li- $x$ Er ( $x = 0.2, 0.8$  wt%) alloys ( $\sim 20 \mu\text{m}$ ) manifest high ductility with elongation larger than 17.0%. The high ductility can be attributed to the synergy effect of solute Li and Er dramatically reducing the  $\text{CRSS}_{\text{non-basal}}/\text{CRSS}_{\text{basal}}$ . The  $\text{CRSS}_{\text{prism}}/\text{CRSS}_{\text{basal}}$  and  $\text{CRSS}_{\text{Py I } \langle a \rangle}/\text{CRSS}_{\text{basal}}$  of Mg-3Li-0.2Er alloy are about 1.29 and 2.27, respectively, which are much lower than that of pure Mg and most commercial Mg alloys.
- (3) Er microalloying enhances alloy ductility. In addition to the easier activation of basal slip caused by more diffuse texture, the better intergranular coordination ability is also responsible for the higher ductility in the higher Er-containing alloy. There is a larger frequency of GBs (18.6%) with  $75^\circ < \theta_s < 90^\circ$  in the Mg-3Li-0.8Er alloy, which enhances intergranular coordination ability by activating more basal-slip-induced prismatic  $\langle a \rangle$  slips.

**Fig. 14** Histograms of misorientation distribution in the **a** Mg-3Li-0.2Er and **b** Mg-3Li-0.8Er alloys



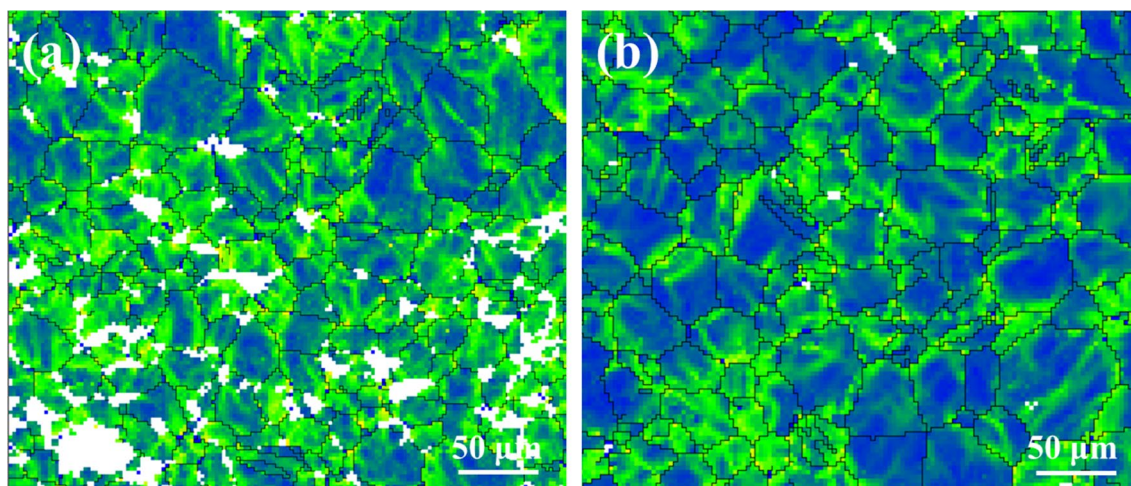


**Fig. 15** Kernel Average Misorientation(KAM) maps in the **a** Mg-3Li-0.2Er and **b** Mg-3Li-0.8Er alloys after 8% tensile strain

**Acknowledgements** This work is financially supported by the Program for Chongqing Talents and China Aeronautical Science Foundation (2023Z0530Q9002).

**Author's contributions** Ruyue Tang—Investigation, Methodology, Data curation, Writing-original draft, Writing-review & editing. Jing Zhang—Investigation, Supervision, Methodology, Data curation, Funding acquisition, Writing – review & editing. Bingcheng Li—Investigation, Methodology, Data curation. Quan Dong—Investigation, Data curation.

**Data availability** Data will be made available on request.

## Declarations

**Competing Interests** The authors declare that they have no known competing financial interests or personal relationships that could have appeared to influence the work reported in this paper.

## References

- Z. Zeng, N. Stanford, C.H.J. Davies, J.-F. Nie, N. Birbilis, Magnesium extrusion alloys: a review of developments and prospects. *Int. Mater. Rev.* **64**(1), 27–62 (2018)
- Z. Wu, W.A. Curtin, The origins of high hardening and low ductility in magnesium. *Nature* **526**(7571), 62–67 (2015)
- K.Y. Xie, Z. Alam, A. Caffee, K.J. Hemker, Pyramidal I slip in c-axis compressed mg single crystals. *Scr. Mater.* **112**, 75–78 (2016)
- Z. Wu, Ahmad, Rasool, Yin, Binglun, Sandloebes, Stefanie, W. Curtin, Mechanistic origin and prediction of enhanced ductility in magnesium alloys. *Science* **359**(6374), 447–452 (2018)
- G. Liu, J. Zhang, G. Xi, R. Zuo, S. Liu, Designing mg alloys with high ductility: reducing the strength discrepancies between soft deformation modes and hard deformation modes. *Acta Mater.* **141**, 1–9 (2017)
- B.Y. Liu, F. Liu, N. Yang, X.B. Zhai, L. Zhang, Y. Yang, B. Li, J. Li, E. Ma, J.F. Nie, Z.W. Shan, Large plasticity in magnesium mediated by pyramidal dislocations. *Science* **365**(6448), 73–75 (2019)
- S. Ganeshan, S.L. Shang, Y. Wang, Z.K. Liu, Effect of alloying elements on the elastic properties of mg from first-principles calculations. *Acta Mater.* **57**(13), 3876–3884 (2009)
- J. Zhang, Y. Dou, G. Liu, Z. Guo, First-principles study of stacking fault energies in Mg-based binary alloys. *Comput. Mater. Sci.* **79**, 564–569 (2013)
- J. Zhang, Y. Dou, H. Dong, Intrinsic ductility of Mg-based binary alloys: a first-principles study. *Scr. Mater.* **89**, 13–16 (2014)
- S. Ando, H. Tonda, Non-basal slips in magnesium and magnesium–lithium alloy single crystals. *Mater. Sci. Forum* **350-351**, 43–48 (2000)
- S.R. Agnew, J.A. Horton, M.H. Yoo, Transmission electron microscopy investigation of  $\langle c+a \rangle$  dislocations in mg and  $\alpha$ -solid solution Mg–Li alloys. *Metall. Mater. Trans. A* **33**(3), 851–858 (2002)
- S. Sandlöbes, M. Friák, S. Zaeferrer, A. Dick, S. Yi, D. Letzig, Z. Pei, L.F. Zhu, J. Neugebauer, D. Raabe, The relation between ductility and stacking fault energies in mg and Mg–Y alloys. *Acta Mater.* **60**(6–7), 3011–3021 (2012)
- S. Sandlöbes, S. Zaeferrer, I. Schestakow, S. Yi, R. Gonzalez-Martinez, On the role of non-basal deformation mechanisms for the ductility of mg and Mg–Y alloys. *Acta Mater.* **59**(2), 429–439 (2011)
- D. Zhang, H. Wen, M.A. Kumar, F. Chen, L. Zhang, I.J. Beyerlein, J.M. Schoenung, S. Mahajan, E.J. Lavernia, Yield symmetry and reduced strength differential in Mg-2.5Y alloy. *Acta Mater.* **120**, 75–85 (2016)
- J. Xu, B. Guan, Y. Xin, G. Huang, P. Wu, Q. Liu, Revealing the role of pyramidal  $\langle c+a \rangle$  slip in the high ductility of Mg–Li alloy. *J. Magnes. Alloy.* (2021). <https://doi.org/10.1016/j.jma.2021.11.012>
- H. Wang, C.J. Boehlert, Q. Wang, D. Yin, W. Ding, Analysis of slip activity and deformation modes in tension and tension-creep tests of cast Mg-10Gd-3Y-0.5Zr (wt pct) at elevated temperatures using in situ SEM experiments. *Metall. Mater. Trans. A* **47**(5), 2421–2443 (2016)
- B. Zhou, Y. Li, L. Wang, H. Jia, X. Zeng, The role of grain boundary plane in slip transfer during deformation of magnesium alloys. *Acta Mater.* **227**, 117662 (2022)
- M. Yuan, J. Zhang, Y. Deng, X. Guo, L. Guan, Mechanism of ductility enhancement of the Mg-8Gd-4Y-1Nd-0.5Si Alloy by multi-directional forging process before extrusion. *Met. Mater. Int.* **29**(5), 1323–1333 (2022)
- H. Wang, C.J. Boehlert, Q.D. Wang, D.D. Yin, W.J. Ding, In-situ analysis of the tensile deformation modes and anisotropy of extruded Mg-10Gd-3Y-0.5Zr (wt%) at elevated temperatures. *Int. J. Plast.* **84**, 255–276 (2016)

20. A. Khosravani, D.T. Fullwood, B.L. Adams, T.M. Rampton, M.P. Miles, R.K. Mishra, Nucleation and propagation of {101-2} twins in AZ31 magnesium alloy. *Acta Mater.* **100**, 202–214 (2015)
21. Z. Jun, J. Bin, Y. Yuan, Q. Wang, M. Yuan, A. Tang, G. Huang, D. Zhang, P. Fusheng, Understanding the enhanced ductility of Mg-Gd with Ca and Zn microalloying by slip trace analysis. *J. Mater. Sci. Technol.* **95**, 20–28 (2021)
22. A.A. Nayeib-Hashemi, J.B. Clark, *Phase Diagram of Binary Magnesium Alloys* (ASM International, Materials Park, 1988)
23. J. Liu, D. Bian, Y. Zheng, X. Chu, Y. Lin, M. Wang, Z. Lin, M. Li, Y. Zhang, S. Guan, Comparative in vitro study on binary Mg-RE (Sc, Y, La, Ce, Pr, Nd, Sm, Eu, Gd, Tb, Dy, Ho, Er, Tm, Yb and Lu) alloy systems. *Acta Biomater.* **102**, 508–528 (2020)
24. W.B. Hutchinson, M.R. Barnett, Effective values of critical resolved shear stress for slip in polycrystalline magnesium and other hcp metals. *Scr. Mater.* **63**(7), 737–740 (2010)
25. C.M. Cepeda-Jiménez, J.M. Molina-Aldareguia, M.T. Pérez-Prado, Effect of grain size on slip activity in pure magnesium polycrystals. *Acta Mater.* **84**, 443–456 (2015)
26. Y.B. Chun, M. Battaini, C.H.J. Davies, S.K. Hwang, Distribution characteristics of in-grain misorientation axes in cold-rolled commercially pure titanium and their correlation with active slip modes. *Metall. Mater. Trans. A* **41A**(13), 3473–3487 (2010)
27. H. Yu, Y. Liu, Y. Liu, D. Wang, Y. Xu, B. Jiang, W. Cheng, L. Huang, W. Tang, W. Yu, Enhanced strength-ductility synergy in Mg-0.5 wt%Ce alloy by hot extrusion. *Met. Mater. Int.* **29**(7), 2109–2116 (2022)
28. J. Zhao, J. Fu, B. Jiang, A. Tang, H. Sheng, T. Yang, G. Huang, D. Zhang, F. Pan, Influence of Li addition on the microstructures and mechanical properties of Mg–Li alloys. *Met. Mater. Int.* **27**(6), 1403–1415 (2019)
29. D. Wu, R.S. Chen, E.H. Han, Excellent room-temperature ductility and formability of rolled Mg–Gd–Zn alloy sheets. *J. Alloys Compd.* **509**(6), 2856–2863 (2011)
30. G. Gottstein, T. Al-Samman, Texture development in pure Mg and Mg alloy AZ31. *Mater. Sci. Forum* **495**, 623–632 (2005)
31. S.L. Couling, J.F. Pashak, L. Sturkey, Unique deformation and aging characteristics of certain magnesium-base alloys. *Trans. ASM* **51**, 94–107 (1959)
32. R. Sánchez-Martín, M.T. Pérez-Prado, J. Segurado, J. Bohlen, I. Gutiérrez-Urrutia, J. Llorca, Molina-Aldareguia, measuring the critical resolved shear stresses in Mg alloys by instrumented nanoindentation. *Acta Mater.* **71**, 283–292 (2014)
33. H. Li, D.E. Mason, T.R. Bieler, C.J. Boehlert, M.A. Crimp, Methodology for estimating the critical resolved shear stress ratios of  $\alpha$ -phase Ti using EBSD-based trace analysis. *Acta Mater.* **61**(20), 7555–7567 (2013)
34. G. Zhu, L. Wang, H. Zhou, J. Wang, Y. Shen, P. Tu, H. Zhu, W. Liu, P. Jin, X. Zeng, Improving ductility of a Mg alloy via non-basal  $\langle a \rangle$  slip induced by Ca addition. *Int. J. Plast.* **120**, 164–179 (2019)
35. K.X. Sun, Y. Zeng, D.D. Yin, F. Gao, L.J. Long, X.Y. Qian, Y.J. Wan, G.F. Quan, B. Jiang, Quantitative study on slip/twinning activity and theoretical critical shear strength of Mg alloy with Y addition. *Mater. Sci. Eng. A* **792**, 139801 (2020)
36. T.R. Bieler, P. Eisenlohr, C. Zhang, H.J. Phukan, M.A. Crimp, Grain boundaries and interfaces in slip transfer. *Curr. Opin. Solid State Mater. Sci.* **18**(4), 212–226 (2014)
37. R. Alizadeh, M. Peña-Ortega, T.R. Bieler, J. Llorca, A criterion for slip transfer at grain boundaries in Al. *Scr. Mater.* **178**, 408–412 (2020)
38. F. Wang, S. Sandlöbes, M. Diehl, L. Sharma, F. Roters, D. Raabe, In situ observation of collective grain-scale mechanics in Mg and Mg–rare earth alloys. *Acta Mater.* **80**, 77–93 (2014)

**Publisher's Note** Springer Nature remains neutral with regard to jurisdictional claims in published maps and institutional affiliations.

Springer Nature or its licensor (e.g. a society or other partner) holds exclusive rights to this article under a publishing agreement with the author(s) or other rightsholder(s); author self-archiving of the accepted manuscript version of this article is solely governed by the terms of such publishing agreement and applicable law.